Optimizing the photocatalytic performance of SnO_2 nanoparticles for methylene blue removal with variation in calcination temperatures

Eka Nurhidayah[1], *Akhmad Herman* Yuwono[1*], *Fairuz* Septiningrum[2], *Fakhri Akbar* Maulana[1], *Donanta* Dhaneswara[1], *Nofrijon* Sofyan[1], *Azizah Intan* Pangesty[1], and *Alfian* Noviyanto[3,4]

[1]Universitas Indonesia, Department of Metallurgical and Materials Engineering, 16424 Depok, Indonesia
[2]Universitas Indonesia, Advanced Materials Research Center, 16424 Depok, Indonesia
[3]Nanotech Indonesia Global, Nano Center Indonesia, 15314 South Tangerang, Indonesia
[4]Universitas Mercu Buana, Department of Mechanical Engineering, 11610 Jakarta, Indonesia

Abstract. In recent years, numerous studies have been conducted to combine tin oxide (SnO_2) with various semiconductor materials to boost its photocatalytic efficiency for water waste treatment, with minimal emphasis placed on intensifying the intrinsic capabilities of pure SnO_2. The primary objective of this study is to enhance the photocatalytic efficiency of pure SnO_2 nanoparticles (NPs) by modifying their morphology, structural, and optical properties. The SnO_2 NPs were synthesized using precipitation method, followed by a calcination process at varying temperatures (non-calcined, 300 °C, and 500 °C). The changes in properties of SnO_2 NPs were investigated utilizing X-ray diffraction (XRD), scanning electron microscopy (SEM), particle size analysis (PSA), Brunauer-Emmett-Teller (BET), and ultraviolet-visible (UV-Vis) spectroscopy. The results indicated that elevating the calcination temperature up to 500 °C resulted in an increase in both the average crystallite size (up to 10.50 nm) and crystallinity (up to 85.28 %). However, the highest photocatalytic efficiency for methylene blue degradation of 84.78 % was obtained from the SnO_2 NPs calcined at 300 °C sample exhibiting the largest surface area of 83.97 m^2g^{-1}. This study affirms that the specific surface area of SnO_2 NPs is a critical factor in their efficacy for degrading dye-contaminated water waste.

1 Introduction

In 2022, an estimated 6.3 billion USD worth of synthetic dyes were distributed in the market, particularly within the textile industry [1]. The textile industries show a preference for synthetic organic dyes over natural dyes due to their economic advantages, which arose from their relatively low purchase costs and ability to provide more uniformity in quality. These organic dyes include Benzene Sulfonate [2], Crystal Violet [3], Malachite Green [4,5], Orange-G [6], Methyl Orange [7], and Methylene Blue [8–10].

* Corresponding author: ahyuwono@eng.ui.ac.id

The inadequate management of organic dye water waste is a significant contributor to environmental pollution, leading to the deterioration of water quality and subsequent negative impacts on the surrounding ecosystem, aquatic life, humans, and other organisms inhabiting the area [5]. It has been reported that at least 4 billion people around the world do not have access to safe, readily drinkable water without the need for additional treatment. Most of these individuals reside in poor countries. However, in some developed countries like France and the United States, there is a growing reluctance among certain populations to consume tap water directly. This reluctance stems from sociocultural factors and concerns about water quality [11]. Furthermore, the consumption of contaminated water has been associated with the development of several health disorders, including gastrointestinal ailments, respiratory infections, brain system disorders, fertility complications, and cancer [12–14].

The worldwide attention and concern regarding water as a fundamental human right, including the water waste treatment systems, are closely linked to the sixth and fourteenth Sustainable Development Goals (SDGs) which aim to ensure universal access to clean water and sanitation, as well as promoting life below water [15,16]. Previously, chemical oxidation processes utilizing ozone, hydrogen peroxide, and chlorine were often chosen for degrading dye-contaminated water waste due to their satisfactory results [17]. However, these processes require relatively high costs, prompting an exploration of Advanced Oxidation Processes (AOP) with or without a catalyst in recent years [18–20], along with other alternatives approaches such as biosorption [21,22], inorganic adsorption [20], and membrane [23] technologies.

Photocatalysis, among various water waste treatment technologies, has been acknowledged as a viable approach for water waste treatment within Advanced Oxidation Processes (AOP) with a catalyst due to its cost-effectiveness, environmental compatibility, lack of polycyclic hydrocarbon emissions, and ability to address various issues related to environmental pollution, particularly in resource-constrained conditions [18,24,25]. This process is applied using photocatalytic materials through chemical reactions triggered by the absorption of photon energy. SiO_2 [26], TiO_2 [27], CeO_2 [28], ZnO [29], Fe_2O_3 [30], dan SnO_2 [8,10,31] are frequently implemented metal oxide photocatalysts for wastewater remediation. For nanoparticles (NPs) to be considered effective photocatalytic materials, they must satisfy several criteria: (i) a significantly high surface area, (ii) the ability to absorb photons in the visible light range, (iii) a low rate of charge recombination, (iv) a low band gap energy (E_g), (v) resistance to agglomeration, and (vi) the capability of being reused [32].

Multiple studies have been conducted to integrate SnO_2 with various semiconductor materials to enhance their photocatalytic efficacy. However, there have been only a few attempts to enhance the inherent capabilities of SnO_2 itself, resulting in minimal improvements in pure SnO_2 or SnO_2-based photocatalysts. At present, it has been observed that SnO_2 materials demonstrate an excellent photocatalytic reaction when exposed to UV irradiation [24]. The synthesis process of SnO_2 nanomaterials with optimal photocatalytic properties has been carried out using several methods, including templating [33,34], electrospinning [35], electrolysis [36], ultrasonic radiation [37], sol-gel [10,38], hydrothermal [39], and precipitation [40–42]. The primary advantages of using precipitation, in comparison to others, are that this method offers (i) a simple procedure, (ii) the use of simple and cost-effective tools, (iii) the utilization of a non-toxic solvent, and (iv) an eco-friendly nature [43,44].

The objective of this study was to determine the optimal calcination temperature required for the synthesis of highly efficient photocatalytic materials capable of degrading organic dyes using the precipitation method. The findings of this study may contribute to a better understanding of the characteristics of enhanced photocatalytic materials, particularly pure SnO_2 or SnO_2-based nanoparticles. As such, the discussion section will be divided into the

crystallographic, morphological, and optical properties, as well as the photocatalytic performance of SnO_2.

2 Materials and Methods

The materials utilized in this experiment, including tin (II) chloride dihydrate ($SnCl_2{\cdot}2H_2O$, Merck), 25 % ammonia solution (NH_4OH, Merck), and distilled water were used without any additional purification.

With an average drop rate of 11.67 ml·min^{-1}, a 0.2 M solution of $SnCl_2{\cdot}2H_2O$ was mixed with 0.8 M of NH_4OH until a milky white homogenous solution was formed. After two days of room temperature precipitation, a white precipitate formed from the mixed solution. This precipitate was then subjected to multiple filtration and purification cycles utilizing deionized water to reduce its pH to 7 (neutral acidity). The precipitate was subsequently dried in an oven at 110 °C for over 3 h and then ground into powder using an agate mortar. To modify the morphology, structure, and optical properties of SnO_2, the synthesized powder underwent further treatment through calcination at temperatures of 300 and 500 °C in a muffle furnace for 3 h, while a non-calcined sample was also prepared for comparison purpose.

The X-Ray Diffraction (XRD, PANalytical X'Pert Pro) in the 2θ range of 20–90 ° with Cu-Kα radiation as the incident beam source was employed to determine the crystal structure and crystallite phase of the powdered SnO_2 samples. The Scanning Electron Microscope–Energy Dispersive X-Ray Spectroscopy (SEM–EDS, ELECMI Inspect F-50) at a magnification exceeding 5000x was used to analyse the surface morphology and the quantity of chemical substances in the samples. The Dynamic Light Scattering (DLS) mode Particle Size Analyzer (PSA, PANalytical Malvern) was employed to measure the particle size of the samples. For this analysis, 0.01 g of SnO_2 powder was dissolved in 10 ml of distilled water. By examining the interaction between nitrogen and SnO_2 samples, the Brunauer-Emmett-Teller (BET, NOVA 1200e) method was used to determine the material's specific surface area, while Barrett-Joyner-Halenda (BJH) method was used to calculate its porosity. The band gap energy (E_g) of the samples was determined using UV-Visual Spectroscopy Diffuse Reflectance Spectroscopy (UV-Vis DRS, Agilent Cary 60).

During the evaluation of photocatalytic performance, a synthetic dye solution containing 10 ppm of methylene blue (MB, $C_{16}H_{18}ClN_3S{\cdot}xH_2O$) in 400 ml of water with a pH of 5 was stirred at 300 rpm and room temperature for 20 min in a dark environment to ensure optimal dispersion. The amount of 30 ml liquid sample was used as the pollutant reference sample. Following the addition of 0.20 gL^{-1} SnO_2 powder, the mixture was continuously stirred in the dark for an additional 20 min, and another liquid sample was collected. The photocatalytic process was then conducted for an additional 100 min under the irradiation of a portable UV sterilization lamp (3×11W). During this time, 30 ml of liquid was collected every 20 min. To separate solid degradation product from the liquid of the photocatalytic result sample, the liquid was centrifuged for 10 min. Afterwards, the samples resulting from the degradation process were evaluated using UV-Visual Spectroscopy (PerkinElmer Lambda 25) and the efficiency (η) was calculated using Eq. (1)

$$\eta\ (\%) = \left(1 - \frac{C}{C_0}\right) \times 100 \quad (1)$$

where C represents the dye concentration, which is directly proportional to the amount of light absorbed by the sample at a given time (t) during the photocatalytic process. C_0 is the absorbance of the 10 ppm MB solution, which served as the dye concentration sample prior to the initiation of photocatalysis [45,46].

3 Results and Discussion

As visually discernible by human observation and basic cameras, the as-synthesized powder sample exhibited a light brown colour. This coloration contrasted with the calcined samples at 300 °C and 500 °C, which appeared pristine white and yellowish white, as displayed in Fig. 1. The discrepancy in colour indicates that the escalation in calcination temperature influences the exothermic properties of the samples, thereby diminishing the oxidation effect when the samples interact with or are exposed to ambient air [47]. Furthermore, calcination at 300 and 500 °C caused the samples to contain less water and other volatile substances, leading to a weight loss of 1.75 and 2.72 %, respectively. Substantiating this observation, da Trindade et al. previously demonstrated the higher concentration of hydroxyl groups and smaller lattice constants in SnO_2 in comparison to samples calcined at 400 and 700 °C [48].

Fig. 1. The visual appearance of (a) as-synthesized SnO_2 powder samples, and after calcination at (b) 300 and (c) 500 °C.

3.1 Crystallographic Properties

As depicted in Fig. 2, the XRD analysis results revealed that the powdered samples exhibited a tetragonal structure and a rutile phase within the polycrystalline nature of SnO_2 [10]. The most prominent diffractogram peaks appeared at approximately 26.54, 33.90, 51.79, 37.88, 65.60, and 54.57 °, corresponding to lattice planes of (110), (101), (211), (200), (301), and (220). These findings align well with the standard pattern represented by ICCD No. 01-077-0472 and JCPDS No. 41-1445 [49,50]. Fig. 2 illustrates that (110) is the predominant orientation growth of SnO_2 samples, followed by (101) and (211), which is a popular occurrence during the synthesis of SnO_2 nanomaterials [40,51,52].

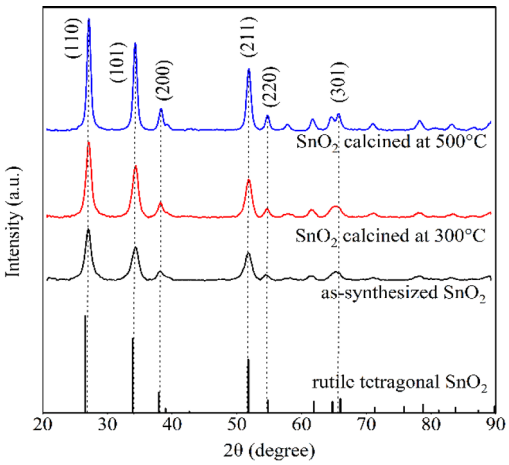

Fig. 2. Diffractogram of SnO_2 samples compared to standard data.

The Debye-Scherrer equation, as denoted in Eq. (2), allows for the calculation of crystallites size (D) and the micro-strains (ε) value through the utilization of Eq. (3) by extracting the full width at half maximum (FWHM) data XRD patterns. However, the non-linear trend observed in the data requires the prediction of these two sets of information using the Williamson-Hall (W-H) plot, as described by Eq. (4).

$$D = \frac{K\lambda}{\beta \cos\theta} \tag{2}$$

$$\varepsilon = \frac{\beta}{4\tan\theta} \tag{3}$$

$$\beta_T = \beta_D + \beta_\varepsilon \Leftrightarrow \beta_T \cos\theta = \varepsilon(4\sin\theta) + \frac{K\lambda}{D} \tag{4}$$

where K represents the grain shape constant (0.94), λ denotes the Cu-Kα wavelength ($\lambda_{Cu\text{-}K\alpha}$) of 1.540598 Å, and θ represents the Bragg's diffraction angle (radians). The FWHM of the highest peaks (radians) is used as broadening parameter (β) when the data is in a linear progression. In the case of nonlinear progression data, the FWHM serves as the total broadening (β_T) [40,50,53]. Additionally, the lattice parameters ($a = b$ and c) and the volume of the unit cell can be determined using Eq. (5), while the degree of crystallinity can be computed using Eq. (6).

$$\frac{1}{d^2} = \frac{h^2+k^2}{a^2} + \frac{l^2}{c^2} \tag{5}$$

$$Crystallinity\ (\%) = \frac{Area\ of\ crystalline\ peaks}{Area\ of\ crystalline\ and\ amorphous\ peaks} \tag{6}$$

The inter-planar distance, denoted as d, is determined using the Bragg's Law, where the (hkl) represents the Miller indices [53,54]. Therefore, Table 1 can be conveniently utilized to present the information, using the XRD results provided in Fig. 2.

Table 1. SnO_2 nanoparticles crystallographic data.

Sample SnO_2	**(hkl)**	**FWHM**	***D* (nm)**	**Lattice Parameters**		**Unit Cell Volume (Å^3)**	**ε (·10^{-3})**	**Crystallinity (%)**
				***a* = *b* (Å)**	***c* (Å)**			
sol-gel dried at 300 °C [55]	(110) (101) (211)	-	7	4.73	3.17	70.92	4.55	-
sol-gel dried at 500 °C [55]	(110) (101) (211)	-	15	4.72	3.18	70.84	4.44	-
as-synthesized	(110) (101) (211)	1.27 1.37 1.36	5.75	4.75	3.19	71.95	-2.79	83.55
calcined at 300 °C	(110) (101) (211)	1.11 1.18 1.19	6.30	4.74	3.20	71.89	-3.28	84.59
calcined at 500 °C	(110) (101) (211)	0.76 0.77 0.85	10.50	4.74	3.20	71.82	-0.64	85.28

The average crystallite size of as-synthesized SnO_2 at 5.75 nm, progressively increased to 10.50 nm upon calcination up to 500 °C. The heat treatment of SnO_2 nanomaterials

typically leads to an increase in the average crystallite size [55]. In contrast to the well-established sol-gel synthesis method, the precipitation-synthesized SnO_2, when subjected to calcination treatment, exhibits a lesser increase in average crystallite size, accompanied by a more pronounced reduction in its micro-strain [55]. The rise in peak intensity, as well as the narrower FWHM and the area under the curves, as depicted in Fig. 2, suggest that increasing the calcination temperature may provide SnO_2 samples with a greater supply of energy, thus facilitating an improvement in their crystallinity [41]. This phenomenon is commonly observed in the calcination processes of SnO_2 [46,56,57], as well as in other metal oxide nanomaterials, such as TiO_2 [58] and ZnO [59]. The SnO_2 nanomaterials synthesized in this study exhibit slightly larger lattice parameters in comparison to the standard data for SnO_2 found in ICCD No. 01-077-0472 [49,50].

The provided data indicates the lattice parameters of $a = b = 4.74$ Å, $c = 3.18$ Å, and a cell volume of 71.45 $Å^3$. These parameters correspond to a space group of $P4_2/mnm$ [10,45,57]. Denoting a reduction in lattice parameters and unit cell volume resulting from an increase in calcination temperature, is also evident in Table 1. These findings align with the brief discussion preceding this subsection. The average crystallite size of these samples is comparable to that of SnO_2 synthesized through basic precipitation (60 °C, 8 h) using various concentration ratios of tin chloride dihydrate/ammonia [60], as well as another precipitation method involving the addition of a 3–6 % HNO_3-ethanol solution to its solvent solution [47]. In comparison to SnO_2-based nanoparticles (NPs) synthesized via co-precipitation and calcined at 600 °C for 4 h, these data indicate smaller sizes [50]. In contrast, these measurements are slightly larger compared to the SnO_2 NPs synthesized via the precipitation method, which involved the addition of H_2O_2 and KOH, followed by a calcination process at 380 °C for 2 h [52].

Furthermore, an increase in the average crystallite size and a decrease in micro-strains (ε) observed in this study also occur in Cu- and Ni-doped SnO_2 NPs synthesized by co-precipitation method with annealed treatment at 500 °C for 2 h [40]. The SnO_2 NPs calcined at 300 °C exhibited the highest micro-strains (ε) value of $3.28 \cdot 10^{-3}$ indicating that their diffraction peaks were more expanded, and their lattice defects were more prominent compared to the other samples [61]. Based on the crystallographic data presented in Table 1, the as-synthesized SnO_2 NPs are suggested as the most promising photocatalysts for the degradation of organic dye wastewater. This recommendation is rooted in their smallest average crystallite size compared to the other samples [51]. Alternatively, the SnO_2 NPs calcined at 500 °C are also a viable choice among the samples because of their highest crystallinity.

3.2 Morphological Properties

The surface morphological properties of SnO_2 NPs were characterized using SEM and are displayed in Fig. 3. The results reveal that spherical granules were formed, exhibiting a tendency for uneven aggregation within a size range of 58.31 nm to 6.46 μm. The formation of spherical materials through isotropic growth, which features uniform orientation growth and minimal energy consumption, has been observed in previous studies conducted by Divya et al. [40] and Letifi et al. [50]. As depicted in Fig. 3, elevated calcination temperatures induce the aggregation of SnO_2 NPs, resulting in the formation of larger and more bulky clusters. This phenomenon is reminiscent of a prior study on co-precipitated SnO_2 at ambient temperature, which demonstrated an average particle size of 10 nm, smaller than the calcined SnO_2 NPs at 400 and 700 °C for 1 h, which formed at 22 and 38 nm, respectively [48].

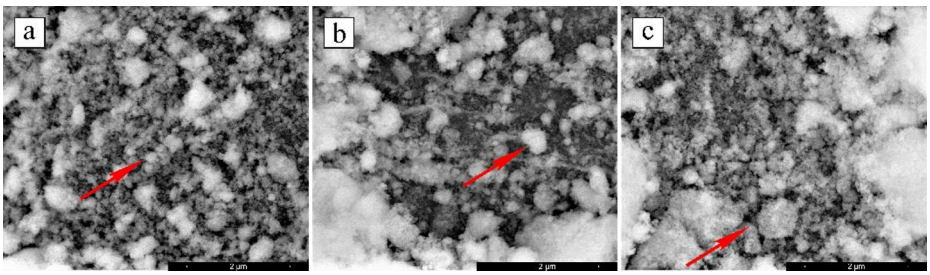

Fig. 3. SEM images of (a) as-synthesized SnO_2 nanoparticles, and after calcination at (b) 300 °C and (c) 500 °C.

In terms of a photocatalytic process, it is commonly held belief that larger clustered materials tend to exhibit lower efficiency [52,58]. For instance, 1 gL^{-1} SnO_2 NPs synthesized via simple co-precipitation were able to completely degrade the water waste within 10 min, whereas the sample calcined at 400 °C required 60 min to achieve a degradation efficiency of up to 99.9% [48]. Therefore, the sample treated with calcination at 500 °C was identified as the least favourable choice for organic dye removal.

To verify this information, quantitative measurements were conducted with DLS mode PSA and found that the particle size of SnO_2 NPs ranged from 68.69 nm to 6.36 µm, as their distribution graph presented in Fig. 4. The results suggest that the particle size distribution of SnO_2 NPs is influenced by the increase in calcination temperature. The particle size distribution had a widening of its range with the lower limit shifting from 79.88 nm to 68.69 nm, while the upper limit expanding from 2.57 µm to 6.36 µm. The shift in the lower limit can be attributed to changes in the mechanical properties of SnO_2 calcined at 500°C. The reduced availability of aqueous or other volatile compounds compared to the other samples makes them more brittle and vulnerable to fragmentation. This, in turn, leads to alterations in the previous structure and the formation of smaller particles [56]. Meanwhile, as naturally hydrophilic materials, it can be understood that as the SnO_2 NPs become drier, their water absorption rate increases, and their susceptibility to agglomerate intensifies [62]. Consequently, the 500 °C calcined sample exhibited a small amount of the largest cluster.

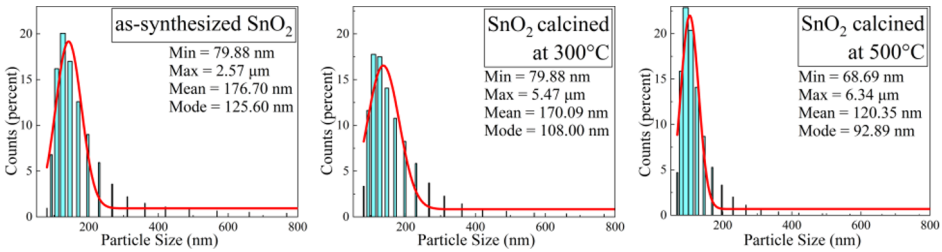

Fig. 4. Particle distribution of SnO_2 nanoparticles with various calcination temperature.

Furthermore, it has been shown that raising the calcination temperature has the potential to enhance the uniformity or homogeneity of the size distribution. This is demonstrated by the narrower Gaussian distribution, as illustrated by the red line, in Fig. 4. Regarding photocatalytic degradation, it is widely acknowledged that smaller particle sizes yield superior results [50]. Kim et al. experimentally compared the catalytic efficiency of 4 mg of precipitation synthesized SnO_2 NPs (with an average diameter size of 4 to 5 nm) and bulk SnO_2 in degrading 10 ppm methylene blue (MB) solutions, revealing that SnO_2 NPs were up to 3.8 times more efficient than their bulk counterparts [52]. This result is primarily attributed to the fundamental concept that smaller particles possess a larger surface area, facilitates the

generation of more electron-hole pairs, and offers increased interaction sites with dye water waste, thereby enhancing the rate of the photocatalytic reaction [50]. Based on particle size perspective, it can be hypothesized that the SnO_2 NPs calcined at 500 °C, possessing an average particle size of 120.35 nm, with the largest proportion (22.86 %) comprised of particles sized at 92.89 nm, could potentially emerge as the most favourable photocatalyst for the removal of methylene blue.

Fig. 5 offers significant insight into the fundamental mechanism of the type IV isotherm [10,63]. The nearly identical adsorption-desorption isotherms curves for each sample suggest that the pores in these samples are classified as closed-ended pores [64,65]. The variation in surface area can be attributed to differences in particle size, which were discussed in the previous paragraph, as well as variances in pore size on their surface, as indicated in Table 2. This BET characterization results provide substantial evidence confirming the classification of the samples as SnO_2 NPs with mesopores in the range size of pores of 3.40–3.84 nm, rendering them suitable for use as functional materials [10,63,66,67].

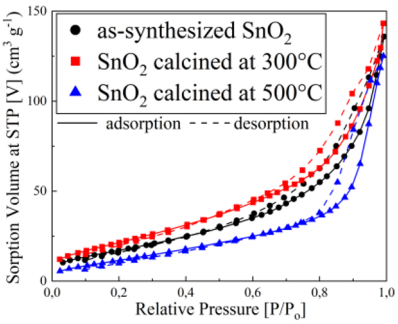

Fig. 5. Adsorption-desorption isotherm of SnO_2 nanoparticles with various calcination temperature.

Table 2. Surface and pore features of SnO_2 nanoparticles.

Sample	Surface Area (m^2g^{-1})	Pore Radius (Å)	Pore Volume (cm^3g^{-1})
as-synthesized	66.60	19.22	0.20
calcined at 300 °C	83.97	17.16	0.21
calcined at 500 °C	48.72	16.99	0.19

The reduction in pore size in the observed samples is attributed to the phenomenon of additional growth induced by an increase in calcination temperature [56], consistent with findings by da Trindade et al., where an increase in calcination temperature up to 700 °C resulted in a smaller pore volume of 0.0481 cm^3g^{-1}, compared to the non-calcined sample with a value of 0.1067 cm^3g^{-1} [68]. However, the reduction in pore volume only correlates with surface area, not with pore radius [69]. The finding differs from the commonly observed phenomenon in which an increase in calcination temperature often leads to a reduction in the surface area of metal oxide nanomaterials [56,70]. The observed result can be explained by the greater total surface area that can potentially be obtained by a majority of SnO_2 NPs calcined at 300 °C (92.89–169.90 nm), as represented in **Fig. 4**, in comparison to as-synthesized (108.00–169.90 nm) or 500 °C (79.88–125.60 nm) variants. The analysis of pores and surface area indicated that SnO_2 NPs calcined at 300 °C, which yielded the highest surface area test result, have been identified as the most effective photocatalytic agents for the removal of MB [67,71–74].

3.3 Optical Properties

The optical properties of SnO_2 NPs were determined by analysing their band gap energy (E_g), which can be calculated using the Tauc plot and the Kubelka-Munk function $F(R)$, as shown in *Figure 6*. This method involves the use of Eq. (7) and Eq. (8).

$$(\alpha hv)^{1/n} = A(hv - E_g) \tag{7}$$

$$F(R) = \frac{K}{S} \Leftrightarrow F(R) = \frac{(1-R)^2}{2R} \tag{8}$$

These equations incorporate various parameters such as the absorption coefficient (α) represented by $F(R)$, the photon energy (hv), proportional constant (A), absorption coefficient (K), scattering coefficient (S), material's reflectance (R), and electron transition propensity factor (n) of the material [7,75]. The value of n is typically 1/2 for direct transitions and 2 for indirect transitions. In this study, a factor of n equal to 2 was used in the calculation [67].

The band gap energy of SnO_2 NPs is intricately linked to their role as photocatalytic materials for the degradation of organic dye pollutants. This connection arises from their need to efficiently absorb photon energy emitted by visible or UV light sources. The absorption graph in Fig. 6(a) reveals a slight blue shift phenomenon, indicating that the light absorption of the calcined SnO_2 NPs shifts towards shorter wavelengths. This suggests that as the calcination temperature increases, the SnO_2 NPs show a greater propensity to absorb high-frequency visible and UV light when compared to the as-synthesized counterparts. However, this data also provides more specific details concerning the highest peak observed in the as-synthesized SnO_2 NPs. It experiences a blue shift from 237.01 to 231.00 nm when compared to the 300 °C sample, while it undergoes a red shift to 240.01 nm when compared to the 500 °C sample. These data align with the estimations obtained from the Tauc plot analysis, in Fig. 6(b), regarding the band gap energy of as-synthesized SnO_2, SnO_2 calcined at 300 °C, and SnO_2 calcined at 500 °C, which are determined to be 3.84, 3.87, and 3.78 eV, respectively.

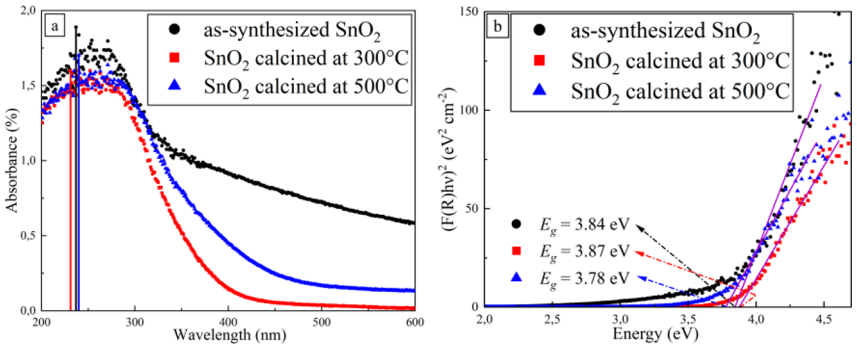

Fig. 6. The (a) absorbance and (b) Tauc plot of SnO_2 nanoparticles with various calcination temperature.

This result partially differs from the widely observed Burstein-Moss effect in semiconductors, which suggest that an increase in the average crystallite and particle size of nanomaterials enhances the electron excitation process at lower energy levels and reduces the band gap energy, allowing to absorp light with longer wavelength [41,47]. In certain conditions, the enlargement of crystallites in nanomaterials, along with the reduction in lattice parameters and unit cell volume, as well as the notable presence of lattice defects, as

previously discussed in the Crystallographic Properties subsection, leads to a greater degree of disorder in the arrangement of valence and conduction bands. This, along with the larger particle size and increased surface defects, results in an observed rise in the band gap energy in SnO_2 NPs calcined at 300 °C [56,61,76]. Meanwhile, the observed red shift and decrease in band gap energy in SnO_2 NPs calcined at 500 °C are commonly attributed to the phenomenon of dehydration, which enhances light absorption and reduces light reflectance, as well as the process of quantum confinement effect [56,60].

The band gap energy of SnO_2 NPs calcined at temperatures equal to or below 500 °C is evidently greater than that of bulk cassiterite materials or rock-like SnO_2 NPs synthesized through a simple solution method [75]. This suggests that the photocatalytic activity of these samples may be more suitable for application under UV-light irradiation [61,77]. The band gap energy level in the present work is deemed more advantageous compared to SnO_2 NPs synthesized using a higher concentration of $SnCl_2$ hydrate, which exhibit band gap energy of no less than 3.93 eV [46,60]. In terms of optical properties, nanomaterials with a narrower band gap energy are more desirable as photocatalysts because they have a higher potential to absorb a broader spectrum of photon energy from visible light. Among the samples, the SnO_2 NPs calcined at 500 °C emerge as the best option [61].

3.4 Photocatalytic Performance

The evaluation of the photocatalytic performance in the degradation of organic dye contaminants in wastewater holds considerable importance for public health and safety. This study used a methylene blue (MB) solution as the water waste sample, and the process and results of photocatalytic activity represented in Fig. 7. Based on the data depicted in Fig. 7(a), it is apparent that, within a 20 min period under dark conditions, there was a notable degradation of MB by 4.11, 26.61, and 23.31 % facilitated by the introduction of 0.20 gL^{-1} of as-synthesized SnO_2 NPs, SnO_2 NPs calcined at 300 °C, and SnO_2 NPs calcined at 500 °C, respectively. In the dark conditions where photochemical reactions are less likely to occur, it was estimated that MB degradation is the result of an adsorption mechanism performed by the respective SnO_2 NP samples [9].

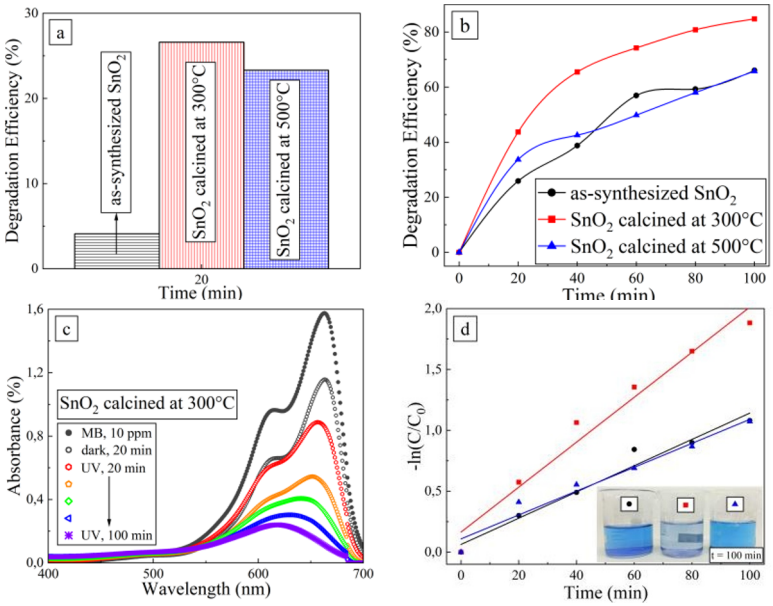

Fig. 7. The (a) dye degradation in dark conditions, (b) dye degradation under UV light efficiency, and (c) example of an absorbance graph of the photocatalysis process, as well as the (d) dye degradation rate curves of applied SnO_2 nanoparticles.

When UV light was introduced into the system, photons with energy higher than the band gap of SnO_2 NPs were absorbed by the materials, triggering a photocatalytic mechanism that led to an exponential increase in degradation efficiency until the 40th min, as shown in Fig. 7(b) [52]. Minor differences observed in the absorbance curves after the 40th min of UV light exposure, as depicted in Fig. 7(c), suggest that the adsorption process no longer contributes significantly, as it did in the beginning. Fig. 7(b) also illustrates that the calcination treatment was effective in reducing the photocatalytic instability initially observed in the as-synthesized SnO_2 NPs.

The performance of SnO_2 NPs calcined at 300 °C was superior to that of the 500 °C variants, which most probably attributed to the decrease in surface area from 83.97 to 48.72 m^2g^{-1}. In the photodegradation of MB using SnO_2 NPs, electron excitation creates holes in the valence band, which serve as oxidizing agents. These holes can directly oxidize MB or oxidize water to produce hydroxyl radicals ($^{\bullet}OH$), which can further oxidize the dye pollutant, ultimately transforming it into non-toxic substances, specifically CO_2 and H_2O [52,74]. The SnO_2 NPs calcined at 300 °C, characterized by their larger surface area, facilitates increased interaction between the holes and MB. The possibility of heightened interaction between the holes and water also promotes the generation of more $^{\bullet}OH$, thereby accelerating the dye degradation process [74].

After 100 min of MB degradation under UV light irradiation, the photocatalytic efficiency of SnO_2 NPs calcined at 300 °C was able to reach 84.78 %, which was significantly higher than the application results of as-synthesized (66.06 %) or calcined at 500 °C (65.78 %). The substantial disparity observed between the photocatalytic results in the dark condition and during UV light irradiation suggests that the photodegradation of MB had a more pronounced influence compared to the adsorption process.

The degradation process utilizing SnO_2 NPs calcined at 300°C demonstrated improved performance compared to the process using SnO_2 NPs calcined at 380°C, as reported by Kim et al, while maintaining a similar ratio of SnO_2 NPs to the MB solution. The utilization of H_2O_2 and KOH in the latter synthesis procedure implies that the current study has

successfully produced a more efficient photocatalyst through a simplified precipitation method [52]. The SnO_2 NPs calcined at 300 °C also outperform Fe_3O_4/SnO_2 nanocomposites, which require higher calcination at 700 °C to achieve optimal performance. This discrepancy in thermal energy requirements highlights the superior efficiency of SnO_2 NPs at a lower calcination temperature [51].

The quantitative performance of MB degradation was evaluated using the kinetic constant (k) through a pseudo-first-order reaction with a simplified Langmuir-Hinshelwood [78], as stated in Eq. (9).

$$-\ln\left(\frac{C}{C_0}\right) = kt \tag{9}$$

As shown in Fig. 7(d), the kinetic constant (k) of MB degradation using SnO_2 NPs calcined at 300 °C (1.85×10^{-2} min^{-1}) surpassed that of as-synthesized (1.08×10^{-2} min^{-1}) or calcined at 500 °C (9.81×10^{-3} min^{-1}). This order aligns precisely with the samples' photocatalytic efficiency, implying that a higher kinetic constant value corresponds to greater photocatalytic efficiency. The kinetic constants observed in this study are significantly higher compared to the SnO_2 nanocrystals synthesized through the precipitation method with a molar ratio of 1/1 of $SnCl_2{\cdot}2H_2O$/NaOH [46].

Given the acidic nature of the wastewater sample (pH = 5) utilized in this investigation, it can be reasonably inferred that the presence of a limited quantity of hydroxyl groups available for conversion to •OH could potentially hinder the photocatalytic effectiveness of the SnO_2 NPs. Consequently, it is reasonable to assume that the application of these SnO_2 NPs to neutral or alkaline wastewater environments might lead to an enhancement in their photocatalytic performance [7,61]. However, considering the prevalent acidic nature of wastewater in our environment, the results presented in this study appear to be sufficient [79]. Moreover, this investigation focuses on the degradation of MB, a cationic dye with a positively charged molecular structure when dissolved in aqueous solutions. Thus, the results are expected to reveal a contrasting pattern compared to anionic dyes like Methyl Orange [7].

4 Conclusion

In summary, the SnO_2 nanoparticles (NPs) have been successfully synthesized through precipitation methods with varying calcination treatment (non-calcined, 300 °C, and 500 °C). Utilizing the BET characterization method, it was observed that the SnO_2 NPs, when calcined at 300°C, displayed the highest specific surface area (83.97 m^2 g^{-1}), despite having a relatively larger particle size in comparison to the SnO_2 NPs calcined at 500°C. The specific surface area of the SnO_2 NPs, calcined at 300°C, facilitates the generation of more electron-hole pairs and offers increased interaction sites with methylene blue water waste. Consequently, this leads to achieving the highest photocatalytic efficiency, reaching up to 84.78 %.

Through the XRD characterization method, it is evident that higher calcination temperatures lead to an increasement in both the average crystallite sizes and the degree of crystallinity in the SnO_2 NPs samples. Employing SEM and PSA characterization methods, an expansion in the range of particle size distribution and distinct levels of homogeneity was observed. Additionally, the UV-Vis DRS characterization method revealed variations in band gap energy corresponding to the increase in calcination temperature. Generally, these sample characteristics do not exert a significantly greater influence on photocatalytic efficiency compared to their specific surface area.

It can be inferred that the optimal condition for the calcination process in the post-treatment procedure of precipitation methods, to improve the photocatalytic properties of SnO_2 nanomaterials, is determined to be 300 °C within the temperature range of 0–500 °C.

This study provides experimental support for the assertion that the performance of the pure SnO_2 photocatalytic mechanism in degrading organic dye pollutants in water is primarily influenced by the specific surface area of the nanomaterials.

The authors are grateful to the Ministry of Education and Culture of the Republic of Indonesia for providing the funds through the *Pendidikan Magister menuju Doktor untuk Sarjana Unggul* (PMDSU) scholarship program. We would like to recognize the Universitas Indonesia, particularly the entire Department of Metallurgical and Materials Engineering, for their invaluable assistance, provision of resources, and infrastructure throughout the entire process of developing this article.

References

1. MarketsandMarkets, in (Pune, 2022)
2. A. R. Galaly, G. van Oost, Plasma Science and Technology **20**, 085504 (2018)
3. F. L. Guzmán-Duque, R. E. Palma-Goyes, I. González, G. Peñuela, R. A. Torres-Palma, J Hazard Mater **278**, 221 (2014)
4. N. Chen, B. Liu, P. Zhang, C. Wang, Y. Du, W. Chang, W. Hong, Inorg Chem Commun **132**, 108848 (2021)
5. S. Hashemian, J Chem **2013**, 1 (2013)
6. Z. Anfar, A. Ait El Fakir, H. Ait Ahsaine, M. Zbair, S. Farsad, F. Morlet-Savary, A. Jada, N. el Alem, New Journal of Chemistry **44**, 9391 (2020)
7. R. Saleh, N. F. Djaja, Superlattices Microstruct **74**, 217 (2014)
8. G. Elango, S. M. Roopan, J Photochem Photobiol B **155**, 34 (2016)
9. F. Sharif, E. P. L. Roberts, Catalysts **10**, 263 (2020)
10. M. A. Ahmed, M. F. A. Messih, E. F. El-Sherbeny, S. F. El-Hafez, A. M. M. Khalifa, J Photochem Photobiol A Chem **346**, 77 (2017)
11. A. K. Biswas, C. Tortajada, Int J Water Resour Dev **35**, 913 (2019)
12. United States Environmental Protection Agency, in *EPA.Gov* (Maryland, 2023)
13. P. Das, R. Horton, The Lancet **391**, 407 (2018)
14. World Health Organization, in (Geneva, 2023)
15. United Nations Development Programme, United Nations Development Programme (2022)
16. Sustainable Development, Departement of Economic and Social Affair (2015)
17. Q. Liu, IOP Conf Ser Earth Environ Sci **514**, 052001 (2020)
18. R. Han, Y. Zhang, Y. Xie, Sep Purif Technol **234**, 116119 (2020)
19. S. M. Albukhari, M. Ismail, K. Akhtar, E. Y. Danish, Colloids Surf A Physicochem Eng Asp **577**, 548 (2019)
20. M. Rani, K. Singh, N. Panwar, J Solgel Sci Technol (2023)
21. A. Sintakindi, B. Ankamwar, Environmental Technology Reviews **10**, 26 (2021)
22. D. Yelatonsev, A. Mukhachev, O. Ivanyuk, Science and Innovation **17**, 83 (2021)
23. D. Naresh Yadav, K. Anand Kishore, B. Bethi, S. H. Sonawane, D. Bhagawan, Environ Dev Sustain **20**, 2065 (2018)
24. C. Sun, J. Yang, M. Xu, Y. Cui, W. Ren, J. Zhang, H. Zhao, B. Liang, Chemical Engineering Journal **427**, 131564 (2022)
25. A. Joseph, A. Vijayanandan, Sustain Chem Pharm **22**, 100453 (2021)
26. S. Stopic, C. Dertmann, I. Koiwa, D. Kremer, H. Wotruba, S. Etzold, R. Telle, P. Knops, B. Friedrich, Metals (Basel) **9**, 708 (2019)
27. V. Bagga, N. Singh, M. Khanuja, M. Rani, D. Kaur, Mater Res Bull **159**, 112109 (2023)
28. S. Balaji, B. K. Mandal, L. V. K. Reddy, D. Sen, Bioengineering **7**, 26 (2020)

29. T. Sansenya, N. Masri, T. Chankhanittha, T. Senasu, J. Piriyanon, S. Mukdasai, S. Nanan, Journal of Physics and Chemistry of Solids **160**, 110353 (2022)
30. D. A. D. N. Dewi, I. N. Simpen, I. W. Suarsa, Jurnal Kimia (Journal of Chemistry) **14**, 82 (2020)
31. International Tin Association, in (Hertfordshire, 2022)
32. M. Á. L. Zavala, S. A. L. Morales, M. Ávila-Santos, Heliyon **3**, E00456 (2017)
33. X. Li, J. Yu, M. Jaroniec, Chem Soc Rev **45**, 2603 (2016)
34. Q. Tian, Y. Chen, W. Zhang, J. Chen, L. Yang, J Alloys Compd **820**, 153382 (2020)
35. P. Zhang, L. Wang, X. Zhang, C. Shao, J. Hu, G. Shao, Appl Catal B **166–167**, 193 (2015)
36. M. Shestakova, P. Bonete, R. Gómez, M. Sillanpää, W. Z. Tang, Electrochim Acta **120**, 302 (2014)
37. H. Ullah, I. Khan, Z. H. Yamani, A. Qurashi, Ultrason Sonochem **34**, 484 (2017)
38. Z. Li, M. Sun, B. Dong, J. Liu, Chem Phys Lett **787**, 139238 (2022)
39. Sh. A. Devi, K. J. Singh, K. N. Devi, *Hydrothermal synthesis of SnO_2 for the photocatalytic degradation of malachite green dye* (AIP Publishing, 2020), p. 030059
40. J. Divya, A. Pramothkumar, S. Joshua Gnanamuthu, D. C. Bernice Victoria, P. C. Jobe prabakar, Physica B Condens Matter **588**, 412169 (2020)
41. P. Khaenamkaew, D. Manop, C. Tanghengjaroen, W. Palakawong Na Ayuthaya, Advances in Materials Science and Engineering **2020**, 1 (2020)
42. P. Suriya, M. Prabhu, E. S. Kumar, K. Jagannathan, Optik (Stuttg) **260**, 168971 (2022)
43. T. Kasuga, M. Hiramatsu, A. Hoson, T. Sekino, K. Niihara, Langmuir **14**, 3160 (1998)
44. W. Matysiak, T. Tański, W. Smok, O. Polishchuk, Sci Rep **10**, 14802 (2020)
45. A. Kar, J. Olszówka, S. Sain, S.-R. I. Sloman, O. Montes, A. Fernández, S. K. Pradhan, A. E. H. Wheatley, J Alloys Compd **810**, 151718 (2019)
46. S. K. Sharma, M. P. C. Kalita, Opt Mater (Amst) **140**, 113845 (2023)
47. D. Liang, S. Liu, Y. Guo, Z. Wang, W. Jiang, C. Liu, W. Ding, H. Wang, N. Wang, Z. Zhang, J Alloys Compd **728**, 118 (2017)
48. L. G. da Trindade, A. C. B. Rocha, V. Teodoro, V. T. da Silva, A. B. Trench, E. Cordoncillo, M. D. Teodoro, S. M. Tebcherani, E. Longo, T. M. Mazzo, Mater Res Bull **153**, 111914 (2022)
49. W. H. Baur, A. A. Khan, Acta Crystallogr B **27**, 2133 (1971)
50. H. Letifi, D. Dridi, Y. Litaiem, S. Ammar, W. Dimassi, R. Chtourou, Catalysts **11**, 803 (2021)
51. V. Paramarta, A. Taufik, R. Saleh, *The role of annealing temperature in photocatalytic performance of Fe_3O_4/SnO_2 nanocomposites* (Institute of Physics Publishing, 2017), p. 012032
52. S. P. Kim, M. Y. Choi, H. C. Choi, Mater Res Bull **74**, 85 (2016)
53. P. Bindu, S. Thomas, Journal of Theoretical and Applied Physics **8**, 123 (2014)
54. A. Khan, A. M. Toufiq, F. Tariq, Y. Khan, R. Hussain, N. Akhtar, S. ur Rahman, Mater Res Express **6**, 065043 (2019)
55. G. Ramanathan, K. R. Murali, J Appl Electrochem **52**, 849 (2022)
56. S. Haq, R. Ehsan, F. Menaa, N. Shahzad, S. U. Din, M. I. Shahzad, W. Rehman, M. Waseem, W. Alrhabi, H. A. Almukhlifi, S. A. Alsharef, Catalysts **12**, (2022)
57. N. E. C. Panthoko, F. Septiningrum, A. H. Yuwono, E. Nurhidayah, F. A. Maulana, N. Sofyan, D. Dhaneswara, L. H. Lalasari, T. Arini, L. Andriyah, F. Firdiyono, Y. W. Ardianto, R. W. Pawan, Metalurgi **38**, 9 (2023)
58. A. Sikirman, J. Krishnan, Applied Mechanics and Materials **575**, 55 (2014)
59. P. Nandi, D. Das, Appl Surf Sci **465**, 546 (2019)
60. M. Saravanakumar, S. Agilan, N. Muthukumarasamy, A. Marusamy, K. Prabaharan, A. Ranjitha, P. Uma Maheshwari, Indian Journal of Physics **88**, 831 (2014)

61. B. Kaleeswaran, Ra.Shanmugavadivu, Brazilian Journal of Physics **53**, 106 (2023)
62. X. Hong, R. Wang, S. Li, J. Fu, L. Chen, X. Wang, J Alloys Compd **816**, 152550 (2020)
63. F. Ambroz, T. J. Macdonald, V. Martis, I. P. Parkin, Small Methods **2**, (2018)
64. K. C. Ng, M. Burhan, M. W. Shahzad, A. Bin Ismail, Sci Rep **7**, 10634 (2017)
65. M. Thommes, K. Kaneko, A. V. Neimark, J. P. Olivier, F. Rodriguez-Reinoso, J. Rouquerol, K. S. W. Sing, in *Pure And Applied Chemistry* (Walter de Gruyter GmbH, 2015)
66. S. Tian, X. Ding, D. Zeng, S. Zhang, C. Xie, Sens Actuators B Chem **186**, 640 (2013)
67. K. Prakash, P. Senthil Kumar, S. Pandiaraj, K. Saravanakumar, S. Karuthapandian, J Exp Nanosci **11**, 1138 (2016)
68. L. G. da Trindade, A. C. B. Rocha, V. Teodoro, V. T. da Silva, A. B. Trench, E. Cordoncillo, M. D. Teodoro, S. M. Tebcherani, E. Longo, T. M. Mazzo, Mater Res Bull **153**, 111914 (2022)
69. Z. X. Sun, T. T. Zheng, Q. B. Bo, M. Du, W. Forsling, J Colloid Interface Sci **319**, 247 (2008)
70. A. Sadeghzadeh-Attar, *Efficient photocatalytic degradation of methylene blue dye by SnO_2 nanotubes synthesized at different calcination temperatures* (2018)
71. H. Benhebal, C. Wolfs, S. Kadi, R. G. Tilkin, B. Allouche, R. Belabid, V. Collard, A. Felten, P. Louette, S. D. Lambert, J. G. Mahy, Inorganics (Basel) **7**, (2019)
72. K. Michalec, A. Kusior, Molecules **26**, (2021)
73. I. Fatimah, G. Purwiandono, M. Husnu Jauhari, A. Audita Aisyah Putri Maharani, S. Sagadevan, W.-C. Oh, R. Doong, Arabian Journal of Chemistry **15**, 103738 (2022)
74. R. A. Husna, Suherman, T. A. Natsir, Results in Engineering **19**, 101253 (2023)
75. V. Perumal, R. Uthrakumar, M. Chinnathambi, C. Inmozhi, R. Robert, M. E. Rajasaravanan, A. Raja, K. Kaviyarasu, J King Saud Univ Sci **35**, 102388 (2023)
76. N. Kamarulzaman, N. D. Abdul Aziz, M. F. Kasim, N. F. Chayed, R. H. Yahaya Subban, N. Badar, J Solid State Chem **277**, 271 (2019)
77. A. Sabarinathan, M. Chinnathambi, R. Jayaprakash, R. Robert, R. Uthrakumar, K. Kaviyarasu, Inorg Chem Commun **156**, 111164 (2023)
78. W. Liu, Q. Kang, L. Wang, L. Wen, Z. Li, Environmental Science and Pollution Research **29**, 51989 (2022)
79. C. Stager, *Our future earth: How planet will change in the next 100,000 years* (duckworth Overlook, Croydon, 2012)